ACS APPLIED MATERIALS & INTERFACES

Research Article

www.acsami.org

Influences of Oxygen Pressure on Optical Properties and Interband Electronic Transitions in Multiferroic Bismuth Ferrite Nanocrystalline Films Grown by Pulsed Laser Deposition

K. Jiang,[†] J. J. Zhu,[†] J. D. Wu,[‡] J. Sun,[‡] Z. G. Hu,*[,†] and J. H. Chu[†]

[†]Key Laboratory of Polar Materials and Devices, Ministry of Education, Department of Electronic Engineering, East China Normal University, Shanghai 200241, People's Republic of China

[‡]Key Laboratory for Advanced Photonic Materials and Devices, Ministry of Education, Department of Optical Science and Engineering, Fudan University, Shanghai 200433, People's Republic of China

ABSTRACT: Bismuth ferrite ($BiFeO_3$) nanocrystalline films with the crystalline size of 27-40 nm have been grown on *c*-sapphire substrates under various oxygen pressures of 1×10^{-4} to 1 Pa by pulsed laser deposition. The X-ray diffraction spectra show that the films are polycrystalline and present the pure rhombohedral phase. It was found that the Raman-active phonon mode E(TO1) shifts towards a higher energy side from 74 to 76 cm^{-1} with increasing oxygen pressure, indicating a larger tensile stress in the films deposited at higher oxygen pressure. The X-ray photoelectron spectroscopy analysis suggests that the concentrations of both Fe^{2+} ions and oxygen vacancies in the $BiFeO_3$ films increase with decreasing oxygen pressure. Moreover, the dielectric functions in the photon energy range of 0.47−6.5 eV have been extracted by fitting the transmittance spectra with the Tauc-Lorentz dispersion model. From the transmittance spectra, the fundamental absorption edge is observed to present a redshift trend with increasing the temperature from 8 to 300 K. Note that the optical band gap (E_g) decreases with increasing the temperature due to the electron-phonon interactions associated with the interatomic distance in the $BiFeO_3$ films. However, the E_g decreases from 2.88 to 2.78 eV with decreasing oxygen pressure at 8 K, which can be attributed to the increment of oxygen vacancies leading to the formation of some impurity states between the valence and conduction band. It can be concluded that the oxygen pressure during the film fabrication has the significant effects on microstructure, optical properties, and electronic band structure modification of the $BiFeO_3$ films.

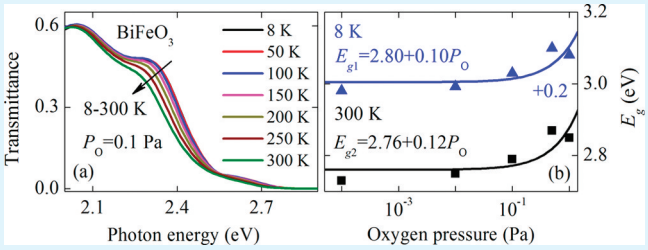

KEYWORDS: *bismuth ferrite, oxygen pressure, electronic transitions, optical properties*

1. INTRODUCTION

Materials that have coupled electric, magnetic, and structural order parameters that result in simultaneous ferroelectricity, ferromagnetism, and ferroelasticity are known as multiferroics.[1,2] These multiferroics materials have attracted a lot of attention in recent years because they can potentially offer a whole range of new applications, including nonvolatile ferroelectric memories, novel multiple state memories, and devices based on magnetoeletric effects.[2−6] Especially, bismuth ferrite ($BiFeO_3$, BFO) is known to be the only perovskite material that exhibits multiferroic at room temperature (RT). At RT, it is a rhombohedrally distorted ferroelectric perovskite with the space group *R*3*c* and a Curie temperature (T_C) of about 1100 K.[1,7−9] It also shows a *G*-type canted antiferromagnetic order below Néel temperature ($T_N \approx 643$ K), in which all neighboring magnetic spins are oriented antiparallel to each other.[8] Recent reports of a large spontaneous polarization (~100 $\mu C/cm^2$) in thin films,[1] bulk ceramics,[10] and single crystals[11] of BFO have lead to an explosion of interest in its growth, electrical, and optical properties. To make BFO useful in actual electrical and optoelectronic devices, we need to further clarify the physical properties, especially for electronic band structure and optical response behavior. Compared to the equivalent ceramic and bulk single crystal, the film materials are expected to yield better sensitivity, faster response, low cost, etc. Therefore, a comprehensive study on BFO films is definitely requisite, which contains fabrication, electrical, and optical properties.

Since the physical properties of BFO films are related to their domain structure and phase states, which is sensitive to the applied stress, composition, and fabrication condition for BFO materials.[12] Many methods, including pulsed laser deposition (PLD),[2,4,7] molecular beam epitaxy (MBE),[5,13] radio-frequency (rf) sputtering,[6,14,15] and chemical solution deposition (CSD)[16] have been employed for the preparation of BFO films. Among them, the PLD technique has the ability to exceed the solubility of magnetic impurity and to permit high quality film grown at low substrate temperature. In addition, the oxygen pressure

Received: September 30, 2011
Accepted: November 21, 2011
Published: November 21, 2011

during the deposition process will significantly affect the crystalline quality and phase purity of the BFO films. Yun et al. have reported the good current-density−applied-voltage characteristics of $BiFeO_3$ thin films deposited at 0.01−0.1 Torr, and the effects of oxygen pressure on their crystal structure and multiferroic properties.[17,18] Wu et al. have found that the BFO film with an oxygen content of about 20% during sputtering had a higher remanent polarization because of its lower leakage current density and an improved phase purity.[19] Furthermore, the different oxygen pressures can lead to the variation of Bi/Fe ratio in BFO film, which closely links with the corresponding ferroelectric properties.[20] Recent studies of photoconductivity,[7] photovoltaic effect,[21] and low open circuit voltage in a working solar device[22] illustrate the potential of polar oxides as the active photovoltaic material. In spite of the promising properties, there are no systematical reports focused on the optical properties of BFO films deposited at various oxygen pressures.

Fortunately, optical spectroscopy is a sensitive and microscopic probe of the nature and size of a band gap, chemical bonding, and hybridization.[5] Moreover, the optical constant, i.e., dielectric functions, can help us gain the related electronic band structure of materials and explain the corresponding experimental results, which will be critical for developing the novel spinelectronic and optoelectronic devices. Although there are some reports on the optical properties of BFO single crystals and films,[9,13,23−26] the optical properties of BFO films grown under different oxygen pressures have not been studied up to date. Yuan et al. have found that the oxygen pressure during cooling after growth, strain-state, and substrate material are important in manipulating the density, diffusion, and distribution of oxygen vacancies.[27] It indicates that the oxygen pressure in the growth process can affect the concentration of oxygen vacancies, which is one of the possible origin of high conductivity in pure BFO films.[28,29] Because oxygen vacancies are unavoidable in the preparation of $BiFeO_3$ samples, both qualitative and quantitative studies about their effects are of great importance. In particular, the oxygen vacancies have a significant influence on the carrier mobility, optical conductivity, and optical response in transition metal oxides.[30] Therefore, the optical properties of BFO films with different oxygen pressures in a wider photon energy region, especially for dielectric functions and optical band gap, should be thoroughly studied in order to exploit its potential applications.

In this paper, the structural and optical properties of BFO nanocrystalline films deposited on *c*-sapphire substrates using the PLD have been investigated by X-ray diffraction (XRD), X-ray photoelectron spectroscopy (XPS), Raman scattering, and temperature-dependent transmittance spectra. The dielectric functions of the films in the near-infrared-ultraviolet (NIR-UV) photon energy region are extracted by reproducing the experimental spectra with the reasonable optical dispersion model. This makes it possible to completely investigate the effects of oxygen pressure on the crystalline phases, dielectric functions, and electronic band structures.

2. EXPERIMENTAL SECTION

Fabrication of $BiFeO_3$ Films. The $BiFeO_3$ films were deposited on *c*-sapphire substrates by the PLD technique. The $BiFeO_3$ targets with a diameter of 3 cm were prepared through a conventional solid state reaction method using reagent-grade Bi_2O_3 (99.9%) and Fe_2O_3 (99.9%) powders. Weighed powders were mixed for 24 h by ball milling with zirconia media in ethanol and then dried at 100 °C for 12 h. The dried powders were calcined at about 680 °C in air for 6 h to form the desired phase, and followed by sintering at about 830 °C for 2 h. Before the deposition of the BFO films, *c*-sapphire substrates need to be cleaned in pure ethanol with an ultrasonic bath to remove physisorbed organic molecules from the surfaces, followed by rinsing several times with de-ionized water. Then the substrates were dried in a pure nitrogen stream before the film deposition. For the BFO growth, the oxygen pressure (P_O = 1 × 10^{-4}, 0.01, 0.1, 0.5, and 1 Pa) was systematically varied while the deposition temperature (T = 450 °C) was fixed. A pulsed Nd:YAG (yttrium aluminum garnet) laser (532 nm wavelength, 5 ns duration) operated with an energy of 60 mJ/pulse and repetition rate of 10 Hz was used as the ablation source. The films were deposited immediately after the target was preablated in order to remove any surface contaminants. The distance between the target and the substrate was kept at 3 cm. The deposition time was set to about 30 min. Finally, the films were annealed at 600 °C in air atmosphere by a rapid thermal annealing process. A detailed preparation of the films can be found in ref 4.

XRD, SEM, XPS, Raman, and Transmittance Measurements. The structure of the films was determined by XRD with Cu Kα radiation operated at 40 kV and 200 mA (D/MAX-2550 V, Rigaku Co.). In this measurement, a vertical goniometer (Model RINT2000) was used and continuous scanning mode (θ-2θ) was selected with a resolution of 0.02° and the 2θ range of 15-75°. The morphological characterization of the films were studied by scanning electron microscopy (SEM). XPS analysis was performed to investigate the surface chemistry of the films using a RBD upgraded PHI-5000C ESCA system (PerkinElmer) with a pass energy of 5 eV for high resolution spectra acquisition with Mg Kα radiation ($h\nu$ = 1253.6 eV). The binding energies were calibrated by using the containment carbon (C 1s = 284.6 eV). The Raman spectra were recorded by a Jobin-Yvon LabRAM HR 800 UV spectrometer, with a He−Ne laser as the excitation light, which is operated at the wavelength of 632.8 nm. The temperature-dependent transmittance spectra were recorded by a double beam ultraviolet-infrared spectrophotometer (PerkinElmer Lambda 950) from 190 to 2650 nm (0.47−6.5 eV) with a resolution of 2 nm. The samples were mounted on a cold stage of an optical cryostat (Janis SHI-4-1) and capable of cooling from 300 to 8 K, which can be set by LakeShore 331 temperature controller.

3. RESULTS AND DISCUSSION

Structural and Morphology Characterizations. The XRD patterns of the films deposited under various oxygen pressures have been shown in Figure 1. As can be seen, some diffraction peaks (012), (104), (110), (202), and (024) are

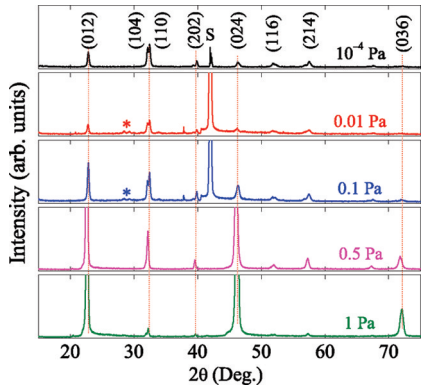

Figure 1. XRD patterns of the $BiFeO_3$ films grown on *c*-sapphire substrates under the oxygen pressure of 1 × 10^{-4}, 0.01, 0.1, 0.5, and 1 Pa, respectively. The symbols (S and *) indicate the observed trace from the sapphire substrate and the impurity phase from Bi_2O_3 for the two BFO films deposited at 0.1 and 0.01 Pa, respectively. Note that the dotted lines show some main diffraction peaks.

observed for the BFO films. The intensities of the (012) and (024) peaks increase with increasing oxygen pressure, suggesting the good crystallinity. Besides the strong features, there are some other weaker diffraction peaks (116), (214), and (036). However, an additional weak peak at 2θ of about 27.8° is detected in the two BFO films deposited at 0.1 and 0.01 Pa, which is also found in the earlier reports.[31−33] These peaks can be associated with the presence of Bi-rich impurity phase Bi_2O_3 due to the similar deposition conditions used in the present study. The results show that the polycrystalline BFO films consist of the perovskite phase with space group *R*3*c* (JCPDS card No. 86-1518) and the second phase appears only in the BFO films deposited under the oxygen pressures of 0.1 and 0.01 Pa. Moreover, the BFO films grown on *c*-sapphire do not exhibit the preferential orientation comparing to the BFO films deposited on $SrTiO_3$ or $DyScO_3$,[2,4,8] which is attributed to the lattice mismatch between the substrates and the BFO films. The average crystalline size *r* can be calculated from the (012) diffraction peak according to the well-known Scherrer equation.[34] Note that the line broadening of the instruments has also been taken into account in the *r* evaluations. It is estimated to about 27, 28, 30, 36, and 40 nm for the BFO films with increasing oxygen pressure, respectively. Note that the crystalline size at higher oxygen pressures (beyond 0.5 Pa) is larger than that at lower oxygen pressures (under 0.1 Pa). The discrepancies are attributed to the different preparation conditions, which may influence the oxygen stoichiometry and subsequently the crystallization.

The surface microstructures of the BFO films deposited under different oxygen pressures are shown in Figure 2. All the films present the uniform granular structures on the *c*-sapphire

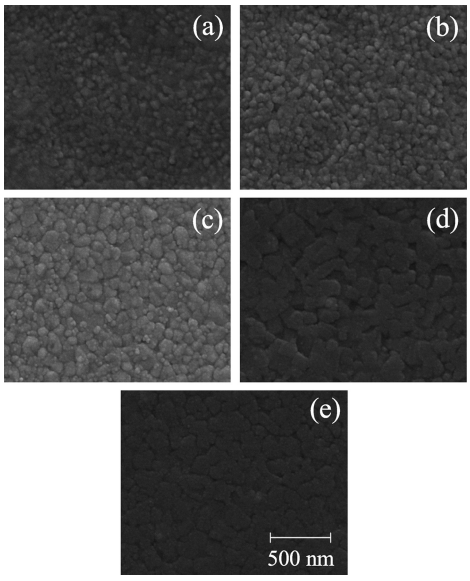

Figure 2. SEM images of the $BiFeO_3$ films deposited at (a) 1×10^{-4}, (b) 0.01, (c) 0.1, (d) 0.5, and (e) 1 Pa. Note that the scale bars for all the images are 500 nm.

substrates. Moreover, the particle size of the BFO films increases with increasing oxygen pressure from 1×10^{-4} to 1 Pa, which agrees well with the results from the XRD analysis. Under the higher oxygen pressures, the surface of the BFO films begins to form the aggregation for the particles, as shown in Figure 2d,e. From the cross-sectional structure, the films have a fluctuating surface and there is a distinct interface between the film and substrate. The thickness of the films gradually increases with increasing oxygen pressure. The remarkable variation of the surface microstructures can obviously affect the optical response such as the transmittance spectra, dielectric function, and optical band gap discussed in the following analysis.

Raman Scattering. Figure 3 shows Raman spectra of the BFO films measured at RT in the range of 50−400 cm^{-1}. Group theory predicts that the BFO films, a rhombohedral

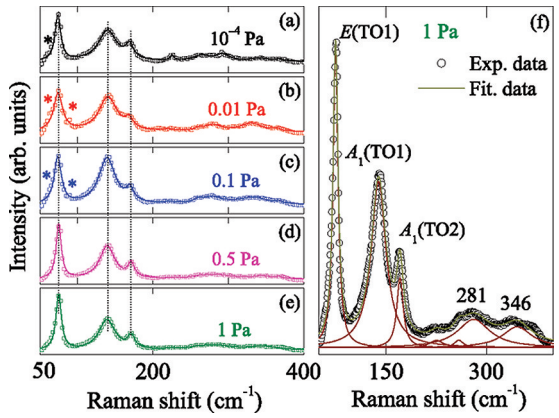

Figure 3. Raman spectra of the $BiFeO_3$ films under the excitation line of 632.8 nm at room temperature. The dashed lines show the positions of Raman-active phonon modes, (f) experimental Raman spectrum (dotted lines) and Lorentzian fitting results (solid lines) of the BFO film deposited at 1 Pa.

perovskite with *R*3*c* space group, should have 18 optical phonon modes: $4A_1 + 5A_2 + 9E$. Among these modes, the A_1 and *E* phonons are Raman- and infrared-active modes, whereas the A_2 modes are optically inactive. The three strong peaks located at around 75, 140, and 170 cm^{-1} are assigned to *E*(TO1), A_1(TO1), and A_1(TO2), respectively. Some weaker peaks at 217, 281, and 346 cm^{-1} are also observed. The results agree well with the previous theoretical and experimental data.[8,35,36] Compared to Raman measurements used by the different laser lines,[8,31] the intensities of the peaks in the present results are quite different, especially for the enhanced *E*(TO1) phonon mode. On the other hand, two additional weak peaks located at about 63 and 89 cm^{-1} for the BFO films deposited under the oxygen pressure of 0.1 Pa are observed in the present work. The two peaks from the impurity Bi_2O_3 phases are associated with the vibration of Bi^{3+} ions, which is also detected by the XRD and XPS measurements.

To further understand the influence of oxygen pressure on the Raman phonon modes for the BFO films, the multi-peak fitting analysis is necessary (see Figure 3f). By fitting the measured Raman spectra and deconvolution of the fitted curves into individual Lorentzian components, the peak position of each component, i.e., the natural frequency of each Raman active mode was obtained. The peak position (ω), full width at half-maximum (Γ), and the intensity (*I*) of the three distinct peaks are presented in Table 1. The changes of the ω, Γ, and I for the *A* and *E* phonon modes significantly depend on the oxygen pressures. Note that the peak position of the *E*(TO1) phonon mode increases from about 74 to 76 cm^{-1} with increasing oxygen pressure. This phonon mode corresponds to the vibrational of Fe and O ions in the *ab* plane from FeO_6 octahedra, which effectively modulates the Fe−O−Fe bond

Table 1. Peak Position (ω), Full Width at Half-maximum (Γ), and Intensity (I) of the Three Phonon Modes Obtained by Fitting Raman Spectra in Figure 3

		E(TO1)			A_1(TOl)			A_1(TO2)		
samples	P_o (Pa)	ω_1 (cm^{-1})	Γ_1 (cm^{-1})	I_1 (au)	ω_2 (cm^{-1})	Γ_2 (cm^{-1})	I_2 (au)	ω_3 (cm^{-1})	Γ_3 (cm^{-1})	I_3 (au)
A	1×10^{-4}	74	14.4	1645	139	29.8	1272	169	13.6	910
B	0.01	75	12.4	1452	141	28.8	1304	170	12.1	747
C	0.1	76	11.7	2484	140	26.7	2442	170	11.9	1214
D	0.5	76	8.5	5017	141	24.4	3229	171	10.7	1856
E	1	76	8.9	4079	140	26.8	2396	170	11.5	1437

angle and Fe−Fe exchange interaction.[8] The increase or decrease of the Raman frequency shift is associated with the tensile/compressive stress that exists in the films. The larger the tensile stress that exists in the film, the higher frequency the Raman shift appears.[12] The results indicate that the BFO films deposited under higher pressure have the larger tensile stress. On the other hand, the A_1(TO1) and A_1(TO2) phonon modes located at the low frequency range are closely related with the Bi−O band.[35] As can be seen from Table 1, the peak positions of the two A phonon modes have a buleshift with increasing oxygen pressures, while the two modes become broadening and the intensities decrease with decreasing oxygen pressure except for the film deposited at 1 Pa. The changes can be attributed to the distortion and defects in the lattice, which is caused by the oxygen vacancies.

XPS Analysis of BFO Films. To identify the chemical bonding of the BFO films, we performed the XPS measurements. For example, Figure 4 shows the overall core level XPS survey spectra of the BFO film deposited at 0.1 Pa. The XPS

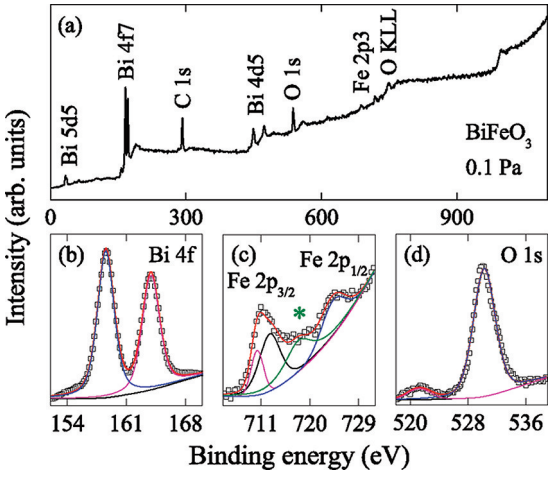

Figure 4. (a) Overall core level X-ray photoelectron spectra for the $BiFeO_3$ film deposited at 0.1 Pa. (b, c, e) XPS spectra of Bi 4f, Fe 2p, and O 1s lines with the Lorentzian-Gaussian dividing peaks analysis. The symbol (*) indicates satellite peak for the Fe^{3+} ions.

spectra of the electron binding energies correspond to Bi, Fe, and O, confirming the phase purity of the films. Figure 4b−d show the Lorentzian-Gaussian dividing peak analysis for Bi 4f, Fe 2p, and O 1s peaks. It is found that Bi $4f_{5/2}$ and Bi $4f_{7/2}$ peak positions are at the binding energy of 158.5 and 163.9 eV, respectively. The binding energy of O 1s is located at 530.2 eV. The 3/2 and 1/2 spin-orbit doublet components of the Fe 2p photoelectron were found to be located at 711.5 and 724.3 eV, respectively. Furthermore, the deconvolution of the $2p_{3/2}$ peaks indicates an additional peak existing around 710.5 eV, as shown in Figure 4c. It indicates that the Fe $2p_{3/2}$ peak corresponds to Fe^{2+} and Fe^{3+} ions for the BFO film with the oxygen pressure of 0.1 Pa.[28,37−39] In addition, the peak located at 718.9 eV (labeled by symbol *) is the satellite peak for Fe^{3+} ions. According to the fitted XPS peak areas and the atomic sensitivity factors for the Bi and Fe elements, the Bi/Fe ratios in the films are quantitatively obtained. For the BFO films deposited at lower oxygen pressures, the ratio is calculated to be about 1.2:1. However, the value increases up to about 1.9:1 at higher oxygen pressures. The increasing trend of the Bi/Fe ratio with the oxygen pressure is consistent with the previous report determined from the energy dispersive X-ray spectroscopy (EDS).[20] This also confirms that the presence of the Bi_2O_3 impure phase observed in XRD and Raman results is reasonable.

The oxygen pressure can affect the formation of oxygen vacancies, which is equivalent to a valence change of Fe from 3+ to 2+: $(O_O^{2-})^x + 2(Fe_{Fe}^{3+})^x = (1)/(2)O_2 + V_O^{\cdot\cdot} + 2(Fe_{Fe}^{2+})'$.[7,39,40] Panels a and b in Figure 5 show the XPS spectrum expanded around the Fe peaks in a range of binding energy

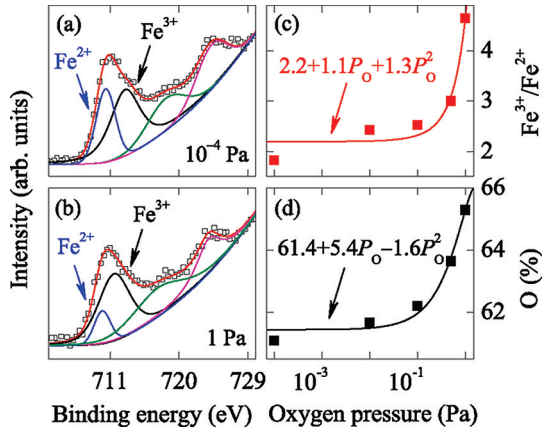

Figure 5. (a, b) Peak-fitting simulations of Fe 2p lines for the $BiFeO_3$ films grown under the oxygen pressure of 1×10^{-4} and 1 Pa, respectively, (c, d) The ratio of Fe^{3+}/Fe^{2+} and content of oxygen in the $BiFeO_3$ films as a function of oxygen pressure from 1×10^{-4} to 1 Pa. The solid lines represent the nonlinear fitting results to guide the eyes.

from 703 to 730 eV for the BFO films deposited at 1×10^{-4} and 1 Pa, respectively. By fitting the peaks for the valence state of Fe ions, the ratios of Fe^{3+}/Fe^{2+} in the BFO films are shown in Figure 5c. It can be concluded that the ratio of Fe^{3+}/Fe^{2+} decreases from 4.6 to 1.9 with decreasing oxygen pressure, and it can be well expressed by the formula: $2.2 + 1.1P_O + 1.3P_O^2$, where P_O stands for the oxygen pressure. From the results, the concentration of the Fe^{2+} ions decreases with increasing oxygen pressure in the fabrication progress, which could be an evidence for the decrease of oxygen vacancies. On the other hand, the

dx.doi.org/10.1021/am201340d | ACS Appl. Mater. Interfaces 2011, 3, 4844−4852

oxygen stoichiometry in the BFO films as a function of the oxygen pressure are shown in Figure 5d. As the oxygen pressure increases from 1×10^{-4} to 1 Pa, the oxygen stoichiometry gradually increases, which also indicates that the oxygen vacancies decrease with the oxygen pressure. The oxygen pressure dependence of the oxygen stoichiometry can be well expressed by $61.4 + 5.4P_O - 1.6P_O^2$. Note that the oxygen contents in all the BFO films are beyond the ideal value of 60%, which is due to the very high surface sensitivity in the XPS measurements. The presence of the moderate oxygen vacancies is consistent with the theoretical calculation and experimental results.[27,30,40] The result suggests that the decreasing of the oxygen pressure can contribute to the increment of oxygen vacancies in the BFO films, and further affect the crystalline structure and electronic structure of the BFO films.

Theoretical Calculation of Transmittance. The inverse synthesis method is based on a phenomenological model fitted to the experimental results. The reliability of the inverse synthesis method mainly depend on the validity of the optical model and the fitting statistics. In order to extract the dielectric functions and other physical parameters of the BFO films deposited on *c*-sapphire substrates, the transmittance spectra were analyzed by a multilayer model with the three-phase layered structure (air/film/substrate). In the wavelength range of 190−2650 nm, the structure modeling of the transmittance was constructed under the assumption that the films and the substrates were treated as isotropic materials. Fortunately, the effect of the surface rough layer, whose value is much less than the film thickness, can be neglected in the evolution of the optical properties. Because the relatively big light spot (about 4 mm in diameter) and vertical/normal incident configuration (about 10°) are used in the present experiments, the transmittance spectra cannot be sensitive to the porous surface layer. At the normal incidence configuration, the transmittance coefficient can be described as: $t = t_{01}t_{12}e^{-i\delta}/(1 + t_{01}t_{12}e^{-i\delta})$, where the partial transmittance coefficient t_{01} (air−film) and t_{12} (film-substrate) are written as $t_{i,i+1} = 2(\tilde{\varepsilon}_i)^{1/2}/(((\tilde{\varepsilon}_i)^{1/2}) + ((\tilde{\varepsilon}_{i+1})^{1/2}))$. The phase factor for the film with thickness d has the form $\delta = 2\pi d((\tilde{\varepsilon}_1)^{1/2})/\lambda$ where λ is the incident wavelength, and the dielectric function of vacuum, the film, and the substrate are $((\tilde{\varepsilon}_0)^{1/2})$ (= 1), $((\tilde{\varepsilon}_1)^{1/2})$, and $((\tilde{\varepsilon}_2)^{1/2})$, respectively. Thus, the spectral transmittance can be readily obtained from $T = \text{Real}[((\tilde{\varepsilon}_2)^{1/2})]tt^*$. It should be emphasized that the absorption from the substrate must be taken into account to calculate the transmittance of the film-substrate system. Therefore, the total transmittance is given by $T = T_{20}T_f\exp(-\alpha_s)/[1 - R_{20}R_f\exp(-2\alpha_s)]$, where T_{20} and R_{20} are the transmittance and reflectance at substrate−air interfaces, respectively. Also, $\alpha_s = 4\pi k_s d_s/\lambda$, d_s is the substrate thickness (0.5 mm in this work) and k_s the extinction coefficient of the substrate, whereas T_f is the overall transmittance from the front side of the film and R_f is the overall reflectance from the back side of the film.[41,42]

It is a challenge to simulate transmittance spectra of semiconductor film in a wider photon energy region because there is a stronger parameter correlation if a complicated dielectric function model is applied. There are some well-known dispersion functions, which are derived from the band parameters and can be used to express the optical response behavior. Among them, the Tauc−Lorentz (TL) model has been successfully applied to express the optical dispersion of the BFO films from the transparent to strong absorption region.[23,24] This model is obtained from the Tauc joint density of states and the standard quantum mechanical or Lorentz calculation for ε_2 (the imaginary part of the complex dielectric function) of a collection of non-interacting atoms. If the multiplied transitions are considered, ε_2 is given by

$$\varepsilon_2(E) = \begin{cases} \dfrac{AE_pC(E - E_0)^2}{(E^2 - E_p^2)^2 + C^2E^2}\dfrac{1}{E} & (E > E_0) \\ 0 & (E \le E_0) \end{cases} \quad (1)$$

and the real part of the dielectric function ε_1 is given by Kramers−Kronig transformation (KKT)

$$\varepsilon_1(E) = \varepsilon_\infty + \frac{2}{\pi}P\int_{E_0}^{\infty}\frac{\xi\varepsilon_2(\xi)}{\xi^2 - E^2}d\xi \quad (2)$$

Equations 1 and 2 depend on the following five parameters: the transition matrix element A, the peak transition energy E_p, the broadening term C, the band gap energy E_0, and the high-frequency dielectric constant ε_∞.[43] A least-squares-fitting procedure employing the modified Levenberg-Marquardt algorithm is used in the fitting. In the method, the fitted parameters are independent on each other and their standard errors are from the experimental uncertainty and instrumental reproducibility. The best-fit model is chosen by simultaneously optimizing the comparison between the experimental and calculated spectra, unbiased estimator for the difference between them, physical likelihood of the solution, and correlation coefficient matrix describing the degree of interdependence between the parameters. The fitting is a process of minimizing the deviation parameter with the optimized values of the five fitting parameters.

NIR-UV Transmittance Spectra and Dielectric Functions. Figure 6a shows the experimental optical transmittance of the BFO films deposited at various oxygen pressures in the photon energy range of 0.47−6.5 eV at 8 K. The spectra can be roughly divided into three specific regions: a transparent oscillating one, a low transmittance one, and a strong absorption one (labeled with I, II, and III, respectively) at higher photon energies.[44] The Fabry−Pérot interference patterns have been observed below the photon energy of 2.0 eV, indicating that the films are transparent in the photon energy region I. On thebais of the simulation, the parameter values of the TL dielectric function model are summarized in

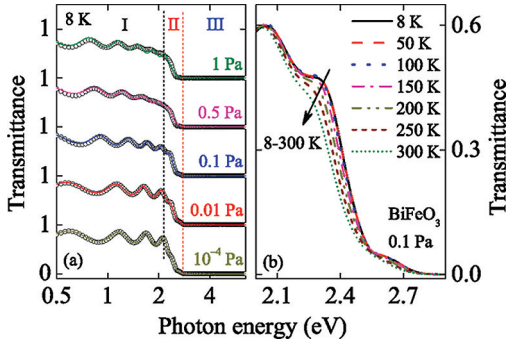

Figure 6. (a) Experimental transmittance spectra (dotted lines) and the best-fit results (solid lines) of the $BiFeO_3$ films from the near-infrared to ultraviolet photon energy region at 8 K. (b) Temperature-dependent transmittance spectra of the $BiFeO_3$ film deposited at 0.1 Pa.

Table 1, and the reproduced transmittance are also plotted by the solid lines in Figure 6a. Note that the calculated spectra can reproduce the measurement data well, indicating that a good agreement between the calculated and experimental spectra is obtained in the entire photon energy region, especially near the fundamental absorption edge. The results show that the TL dispersion function is suitable to express the optical response of the BFO films from 0.47 to 6.5 eV.

The absorption edge is near the end of the interference oscillations and located in the photon energy region II. The spectra of the BFO films in this region show a blueshift, which cannot be clearly judged only in the experimental data. This is because the interference pattern in the films is overlapped with the absorption edge. In addition, the interference in the substrate can also influence the shape of bands and the background of spectra for the different films. Therefore, the fitting calculation with the physical dispersion model is necessary to exactly derive the band gap and optical functions. Of course, the fitting quality strongly depends on the selected dispersion model and structural model. It should be emphasized that the effects from the substrate can be avoided because the optical response of the substrate, such as optical constants, has been considered in the simulations. As an example, the enlarged band gap region of experimental transmittance spectra with different temperature for the BFO films deposited at 0.1 Pa are shown in Figure 6b. With increasing temperature, the absorption edge has an obvious shift toward the lower photon energy. The negative temperature coefficient has been observed for both BFO films and some other semiconductor materials.[4,45] Note that the BFO films exhibit two broadening shoulder characteristics in this region and the intensities becomes much stronger with decreasing the temperature. The shoulder structures in the transmittance spectra corresponds to the p−d and d−d charge-transfer (CT) transitions rather than the inter-band transitions in BFO films.[9] In addition, the small shoulder centered at ∼2.5 eV has been observed in the earlier investigations.[2,13,14,46] Hauser et al. attributed the feature to defect states, which is caused by the oxygen vacancies,[14] while Pisarev et al. pointed that it is an intrinsic nature related to a low-lying $t_{1g}(\pi) \rightarrow t_{2g}$ CT transition typical for all the ferrites with octahedral FeO_6 centers.[46] For the other four films deposited under various oxygen pressures, the presence of the features can also be observed, indicating that the oxygen vacancies induced by the different oxygen pressures have a weak relationship to the feature. Therefore, it can be safely concluded that the dipole-forbidden $t_{1g}(\pi) \rightarrow t_{2g}$ CT transition results in the 2.5 eV shoulder, and the transition becomes much stronger with decreasing the temperature. Obviously, the optical properties obtained by the transmittance spectra can be used to verify the predictions from the electronic structure calculations.

The dielectric functions of the BFO films derived from fitting the transmittance spectra are shown in Figure 7. Compared to the theoretical calculations and experimental results,[9,23,30,47] the variation trend is similar, whereas the derived dielectric functions are slightly different at some photon energies. The ε_2 is almost zero at the photon energy under 2.5 eV, whereas the ε_1 is about 5.0 in this region. With increasing the photon energy, some peaks appear in the dielectric function spectra. The value of ε_2 is close to 2.0 at higher photon energy for the five samples, which is less than those reported.[23,26,47] It can be attributed to the different morphology and quality of the films or the experiment measurements. Owing to the sharp variations

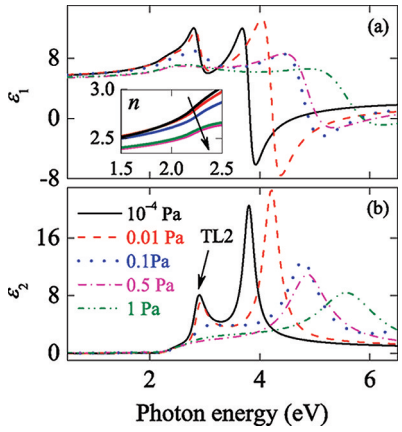

Figure 7. Evolution of (a) real part ε_1 and (b) imaginary part ε_2 of the dielectric functions for the $BiFeO_3$ films deposited at various oxygen pressures. The inset shows the variation of refractive index n in the vicinity of the photon energy of 2.0 eV. The arrows indicate the increase trend for the oxygen pressure from 1×10^{-4} to 1 Pa. The TL2 electronic transitions features can be identified in the imaginary part of the dielectric function.

of the ε_1 and ε_2 in the photon energy range of 3−6.5 eV, one can exclude the case that the ε_1 and ε_2 are almost zero at the same time because it is physically not reasonable. Nevertheless, more sensitive spectral measurement, such as spectroscopic ellipsometry, could be desirable to determine these optical properties in the wide energy range. Clearly, the dielectric functions in present work shift to higher energy as the oxygen pressure increases, especially for the high photon energy region beyond 3.0 eV. On the other hand, the refractive index n of the BFO films at the photon energy of 2.0 eV gradually decreases with the oxygen pressure, as shown in the inset of Figure 7a. It is well known that the refractive index is related to the packing density (σ) and polarizability (P_m) of a given material by the following Lorentz−Lorentz relation: $(n^2 - 1)/(n^2 + 2) \propto (C_A P_m \sigma)/m$. Here, C_A is Avogadro's constant and m is the molecular weight.[48] Therefore, the variation in the refractive index could be ascribed to changes of packing density and/or polarizability. Because the BFO films were deposited with different oxygen pressures, the larger refractive index indicates a higher film packing density owing to the similar polarizability. It indicates that the BFO film deposited at 1×10^{-4} Pa is much denser and has a relatively high packing density. In the imaginary part of the dielectric function, ε_2 (Figure 7b), the transition points corresponding to the fitting parameter values (see Table 2) can be distinctly identified. The transition points are effected by the oxygen pressure, especially in the higher photon energy region. Therefore, from the above considerations, we can conclude that the dielectric functions of the BFO films are influenced by the oxygen pressure.

Effect of Temperature on Optical Band Gap. Previous theoretical calculations and experiments have a common conclusion: the BFO is a direct band gap material.[7,49] The optical band gap (E_g) of the BFO films is one of the important parameters, which is calculated by considering a direct transition from the valence band (VB) to the conduction band (CB) when the photon energy falls on the materials. In the BFO system, the VB is formed predominantly by the O 2p states hybridized with the Fe 3d and Bi 6p states, whereas the lowest CB is mainly composed of the Fe 3d orbital. It should be emphasized that because of the splitting of the Fe 3d

Table 2. Parameter Values of the TL Dispersion Model for the BFO Films with Different Oxygen Pressures Obtained by Fitting the Transmittance Spectra in Figure 6

				TL1 (eV)				TL2 (eV)				TL3 (eV)				TL4 (eV)			
samples	P_o (Pa)	thickness (nm)	ε_∞	A_1	E_{p1}	C_1	E_{01}	A_2	E_{p2}	C_2	E_{02}	A_3	E_{p3}	C_3	E_{03}	A_4	E_{p4}	C_4	E_{04}
A	1×10^{-4}	432	2.5	153	1.8	1.8	2.2	75	2.7	2.0	2.4	4.9	4.3	0.3	0.8	20	5.3	9.0	4.9
B	0.01	449	2.5	151	1.8	1.6	2.2	103	2.8	0.4	2.6	6.2	4.4	0.4	0.2	19	5.4	7.6	3.7
C	0.1	572	2.6	166	1.9	1.2	2.3	86	2.8	0.5	2.5	7.9	5.0	0.7	0.1	9.0	5.8	1.2	2.8
D	0.5	640	2.8	151	1.7	1.4	2.3	60	2.8	0.2	3.3	5.5	4.8	5.0	3.2	8.7	5.7	1.5	0.1
E	1	662	2.8	148	1.7	1.8	2.2	59	2.9	0.2	2.6	8.0	4.2	4.0	2.7	9.0	5.5	1.2	0.1

conduction bands into t_{2g} and e_g subbands, the lowest CB arises from the threefold degenerate Fe 3d t_{2g} orbital, which has lower energy than the twofold degenerate Fe 3d e_g orbital.[46] The absorption coefficient related E_g of the BFO films can be determined according to the Tauc's law: $(\alpha E)^2 = B(E - E_g)$, where B is a constant, α and E are the absorption coefficient and incident photon energy, respectively. For the allowed direct transition, the straight line between $(\alpha E)^2$ and E will provide the value of the band gap, which is extrapolated by the linear portion of the plot to $(\alpha E)^2 = 0$. The E_g is estimated to 2.74 and 2.86 eV corresponding to the BFO films deposited at 1×10^{-4} and 1 Pa, respectively. The results agree well with the previous theoretical prediction and are close to the experimental estimations.[2,4,7]

The temperature dependence of the E_g for the BFO films deposited at different oxygen pressures are plotted in Figure 8a. The energy decreases monotonically as the temperature

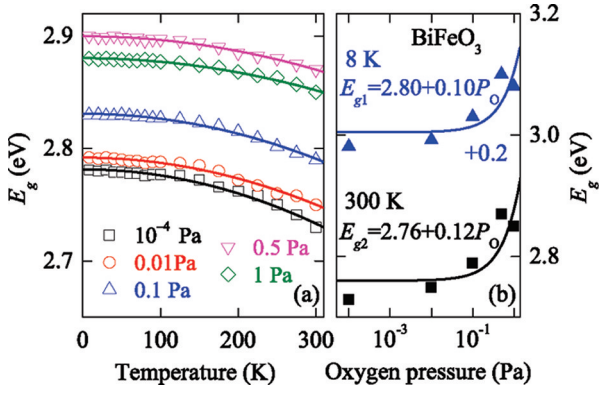

Figure 8. (a) Temperature dependence of the optical band gap energies (dotted curves) and Varshni model fitting results (solid curves) for the $BiFeO_3$ films grown under the oxygen pressures from 1×10^{-4} to 1 Pa. (b) Oxygen pressure dependence of the optical band gap energies for the $BiFeO_3$ films at 8 and 300 K. The solid lines represent the linear fitting results to guide the eyes.

increases, which can be described by the Varshni's equation:

$$E_g(T) = E(0) - \frac{T^2\gamma}{T + \beta} \quad (3)$$

where γ and β are constant and $E(0)$ is the band gap at 0 K.[50,51] For the BFO film deposited at 0.1 Pa, the fitting result indicates that the $E(0)$ value is about 2.83 eV, which is higher than that prepared on $SrTiO_3$ substrate (2.69 eV toward 0 K).[4] The E_g decreases from 2.83 to 2.79 eV, corresponding to the increasing temperature from 8 to 300 K. Note that the redshift value of the E_g is larger than that reported on BFO films by Basu et al. (28 meV).[7] The differences can be attributed to the crystalline quality caused by the preparation progress and various substrates. It is well known that the electron-phonon interactions effectively determine the shrinkage in the value of E_g with the temperature, rather than the thermal expansion of the lattice.[45,52,53] The longitudinal phonons change the interatomic distance along the direction of their propagation with increasing the temperature, resulting in the narrowing of the band gap, while the direct effects due to thermal band-to-band excitations are negligible in the experimental temperature range. The decrease of the E_g can be attributed to the interatomic distances with increasing changes in the lattice, which arises from the electron-lattice interactions.[54] Therefore, the lattice constant of the BFO films is changed because of the dilatation of the lattice and the shortening of interatomic distances, leading to the shifting of the energy levels.

Influence of Oxygen Pressure on Electronic Transitions. For comparison, the parameter values of the TL dielectric function model for the BFO films with different oxygen pressure are summarized in Table 2. The thickness of the BFO film increases from 432 to 662 nm with increasing oxygen pressure by fitting the transmittance spectra recorded at 8 K, which is consistent with the results from SEM. It indicates that the growth velocity is different under changing oxygen pressure during the deposition. In addition, the ε_∞ of the BFO films has a positive correlation to the oxygen pressure. Generally, the parameter ε_∞ accounts for the so-called high-frequency limit. Therefore, the dielectric function model should be extrapolated to shorter wavelengths than those studied here. However, it is nearly impossible that the TL dispersion model can completely explain the complicated behavior of many high-energy transitions in semiconductor/dielectric materials, where an approximate relation proportional to the quartic wavelength is necessary. As the previous discussions, the higher oxygen pressure results in a larger crystalline size of the BFO films. The rhombohedral distortion is reduced by decreasing crystalline size accompanied with decreasing polarization inferred from atomic displacements. There, the ε_∞ increment can be attributed to the size dependent effects, which also affect the crystal symmetry and Neel temperature for the BFO films.[55,56] To clarify the phenomena, the spectral experiments extending the higher photon energy are requisite.

The number of optical transition is related to the physical properties of the BFO films. Based on the previous theoretical calculations and experimental observations, four transitions at the photon energy from ultraviolet to near-infrared and the assignments have been widely accepted.[7,23,46] In order to further understand the origination of the transitions, the schematic diagram of electronic band structures and the four electronic transitions are summarized in Scheme 1. The TL1

optical transition peak is located at about 1.8 eV, which is consistent with assignment as on-site Fe^{3+} crystal-field transition ($^6A_{1g} \rightarrow {}^4T_{2g}$ excitation).[38,49,57] The triply degenerate $^4T_{2g}$ electronic level splits into two crystal-field levels having A and E character due to a reduction in symmetry. As the presence of the oxygen vacancies associated with oxygen pressure, the lattice of the BFO films may be changed slightly, which can lead to the decrease of TL1 transition energy from 1.9 to 1.7 eV at higher oxygen pressures. The TL2 transition energy, which affect the shape of the absorption edge of the BFO films, increases with increasing oxygen pressure. The peak can be attributed to the d−d transitions between the Fe 3d valence and conduction bands.[2,47] The shift is due to the different electronic band structures in the BFO films caused by increasing oxygen pressure. The TL3 and TL4 transitions in higher photon energy region have been identified as a minority channel dipole-allowed O 2p to Fe 3d charge transfer excitation and a strongly hybridized majority channel O 2p + Fe 3d → Bi 6p state excitation, respectively.[4,13,47] With increasing oxygen pressure, the CT energies of the two transitions increase first and then decrease. It can be concluded that the transition energies have a blueshift at lower oxygen pressures, while a redshift at higher oxygen pressures except for the TL2 transition. The effects from the oxygen pressure play an important role in the electronic band structure modification, and further affect the optical response of the BFO films, as shown in Figure 7.

Scheme 1. Schematic Representation of the Electronic Band Structure for the $BiFeO_3$ Films[a]

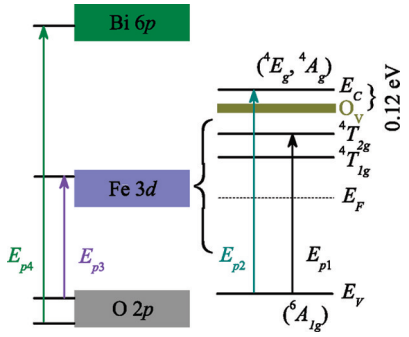

[a]Note that E_C, conduction band; E_V, valence band; E_F, Fermi energy level; O_V, defect states associated to oxygen vacancies, and the four electronic transitions assigned by the solid arrows.

On the other hand, with decreasing oxygen pressure, the band gap energies of the BFO films gradually decreases, from 2.88 to 2.78 eV at 8 K and from 2.85 to 2.73 eV at RT, as shown in Figure 8b. The band gaps increase linearly with the oxygen pressure and these linearities are found as $E_{g1}(P_O) = 2.80 + 0.10P_O$ at 8 K and $E_{g2}(P_O) = 2.76 + 0.12P_O$ at RT. In addition, the redshift value of the E_g with the temperature decreases as the oxygen pressure increases, from 50 meV at 1×10^{-4} Pa to 30 meV at 1 Pa. Furthermore, the band gap narrowing coefficients (dE_g/dT) are calculated to be -4.4×10^{-4} and -2.0×10^{-4} eV/K at RT for the BFO films deposited at 10^{-4} Pa and 1 Pa, respectively. The results indicate that the electronic structures of the BFO films with different oxygen pressures change strongly. As previous discussions (Figure 5), the concentrations of oxygen vacancies and Fe^{2+} ions increase with decreasing oxygen pressure. Some impurity states caused by the presence of oxygen vacancies can be formed in the gap. Thus there is a significant decrease in the band gap energies of the BFO films deposited under lower oxygen pressures. Furthermore, the disproportion of Fe ions for the BFO films caused by the various oxygen vacancies can lead to an asymmetry between spin-up and spin-down Fe states. The Fe^{3+} ion shows a d^5 configuration, with a filled t_{2g} orbital only in one spin channel, while the Fe^{2+} ion shows a d^6 configuration, with a filled t_{2g} orbital in one spin channel and a partially filled t_{2g} orbital in the other channel.[30] Therefore, the Fe states in the BFO films change strongly because of the different states caused by the disproportion of the Fe^{3+} and Fe^{2+} ions. This is to be expected, according to the densities of states,[30] the valence states (d electrons) shift toward the Fermi level and the conduction states shift away from the Fermi level with decreasing oxygen pressure. However, the presence of the impurity states can lead to the decrease of the E_g for the BFO films grown at lower oxygen pressures. Therefore, the increment of the band gap energy in the BFO films with the oxygen pressure can be attributed to the combined effects from the reduce of oxygen vacancies and Fe^{2+} ions.

4. CONCLUSION

The $BiFeO_3$ nanocrystalline films, which consist of perovskite single phase with space group *R*3*c*, have been grown on *c*-sapphire substrates by PLD. It was found that the crystalline size of the BFO films increases from 27 to 40 nm with increasing the oxygen pressure from 1×10^{-4} to 1 Pa. The Raman spectra analysis show that the frequency and intensity of the *E* and *A* phonon modes increase with the oxygen pressure. However, the three modes become broadening with decreasing oxygen pressure except for the film deposited at 1 Pa. From the XPS analysis, the coexistence of Fe^{2+} and Fe^{3+} ions could be inferred in all the samples. The ratio of Fe^{3+}/Fe^{2+} decreases from 4.6 to 1.9 with decreasing oxygen pressure. In addition, the concentration of oxygen vacancies increases with decreasing oxygen pressure, and was expected to affect the crystalline structure, electronic structure and optical band gap. From the transmittance spectra, the small absorption shoulder located at about 2.5 eV can be assigned to a dipole-forbidden p−d CT transition $t_{1g} \rightarrow t_{2g}$. The dielectric functions of the BFO films, which can be obtained from fitting the transmittance spectra, have been significantly influenced by the oxygen pressure. For the films deposited under lower oxygen pressures, some impurity states from the oxygen vacancies are formed in the gap and result in the decrease of the optical band gap. The introduction of Fe^{2+} ions can induce a local structure distortion and strongly change the Fe states, which is useful for the electronic band structure modification. The present results demonstrate that the oxygen pressure has a significant effect on the structural and optical properties of pulsed laser deposited epitaxial BFO films, which is crucial for future applications of BFO-based optoelectronic and photovoltaic devices.

AUTHOR INFORMATION

Corresponding Author

*Tel.: +86-21-54345150. Fax: +86-21-54345119. E-mail: zghu@ee.ecnu.edu.cn.

ACKNOWLEDGMENTS

This work was financially supported by Natural Science Foundation of China (Grants 10DJ1400201, 10SG28, and

11520701300), Major State Basic Research Development Program of China (Grants 2011CB922200 and 2007CB924901), Program of New Century Excellent Talents, MOE (Grant NCET-08-0192) and PCSIRT, Projects of Science and Technology Commission of Shanghai Municipality (Grants 10DJ1400201 and 10SG28), and The Program for Professor of Special Appointment (Eastern Scholar) at Shanghai Institutions of Higher Learning.

REFERENCES

(1) Wang, J.; Neaton, J. B.; Zheng, H.; Nagarajan, V.; Ogale, S. B.; Liu, B.; Viehland, D.; Vaithyanathan, V.; Schlom, D. G.; Waghmare, U. V.; Spaldin, N. A.; Rabe, K. M.; Wuttig, M.; Ramesh, R. *Science* **2003**, *299*, 1719−1722.
(2) Himcinschi, C.; Vrejoiu, I.; Friedrich, M.; Nikulina, E.; Ding, L.; Cobet, C.; Esser, N.; Alexe, M.; Rafaja, D.; Zahn, D. R. T. *J. Appl. Phys.* **2010**, *107*, 123524.
(3) Park, T. J.; Sambasivan, S.; Fischer, D. A.; Yoon, W. S.; Misewich, J. A.; Wong, S. S. *J. Phys. Chem. C* **2008**, *112*, 10359−10369.
(4) Li, W. W.; Zhu, J. J.; Wu, J. D.; Gan, J.; Hu, Z. G.; Zhu, M.; Chu, J. H. *Appl. Phys. Lett.* **2010**, *97*, 121102.
(5) Xu, X. S.; Ihlefeld, J. F.; Lee, J. H.; Ezekoye, O. K.; Vlahos, E.; Ramesh, R.; Gopalan, V.; Pan, X. Q.; Schlom, D. G.; Musfeldt, J. L. *Appl. Phys. Lett.* **2010**, *96*, 192901.
(6) Wu, J. G.; Wang, J.; Xiao, D. Q.; Zhu, J. G. *ACS Appl. Mater. Interfaces* **2011**, *3*, 3261−3263.
(7) Basu, S. R.; Martin, L. W.; Chu, Y. H.; Gajek, M.; Ramesh, R.; Rai, R. C.; Xu, X.; Musfeldt, J. L. *Appl. Phys. Lett.* **2008**, *92*, 091905.
(8) Singh, M. K.; Katiyar, R. S. *J. Appl. Phys.* **2011**, *109*, 07D916.
(9) Choi, S. G.; Yi, H. T.; Cheong, S. W.; Hilfiker, J. N.; France, R.; Norman, A. G. *Phys. Rev. B* **2011**, *83*, 100101.
(10) Shvartsman, V. V.; Kleemann, W.; Haumont, R.; Kreisel, J. *Appl. Phys. Lett.* **2007**, *90*, 172115.
(11) Lebeugle, D.; Colson, D.; Forget, A.; Viret, M.; Bonville, P.; Marucco, J. F.; Fusil, S. *Phys. Rev. B* **2007**, *76*, 024116.
(12) Yang, Y.; Sun, J. Y.; Zhu, K.; Liu, Y. L.; Wan, L. *J. Appl. Phys.* **2008**, *103*, 093532.
(13) Chen, P.; Podraza, N. J.; Xu, X. S.; Melville, A.; Vlahos, E.; Gopalan, V.; Ramesh, R.; Schlom, D. G.; Musfeldt, J. L. *Appl. Phys. Lett.* **2010**, *96*, 131907.
(14) Hauser, A. J.; Zhang, J.; Mier, L.; Ricciardo, R. A.; Woodward, P. M.; Gustafson, T. L.; Brillson, L. J.; Yang, F. Y. *Appl. Phys. Lett.* **2008**, *92*, 222901.
(15) Wu, J. G.; Wang, J.; Xiao, D. Q.; Zhu, J. G. *ACS Appl. Mater. Interfaces* **2011**, *3*, 2504−2511.
(16) Singh, S. K.; Maruyama, K.; Ishiwara, H. *J. Phys. D: Appl. Phys.* **2007**, *40*, 2705−2709.
(17) Yun, K. Y.; Noda, M.; Okuyama, M. *Appl. Phys. Lett.* **2003**, *83*, 3981−3983.
(18) Yun, K. Y.; Noda, M.; Okuyama, M.; Saeki, H.; Tabata, H.; Saito, K. *J. Appl. Phys.* **2004**, *96*, 3399−3404.
(19) Wu, J. G.; Wang, J.; Xiao, D. Q.; Zhu, J. G. *Phys. Status Solidi* **2011**, *5*, 190−192.
(20) You, L.; Chua, N. T.; Yao, K.; Chen, L.; Wang, J. *Phys. Rev. B* **2009**, *80*, 024105.
(21) Yang, S. Y.; Martin, L. W.; Byrnes, S. J.; Conry, T. E.; Basu, S. R.; Paran, D.; Reichertz, L.; Ihlefeld, J.; Adamo, C.; Melville, A.; Chu, Y. H.; Yang, C. H.; Musfeldt, J. L.; Schlom, D. G.; Ager, I. J. W.; Ramesh, R. *Appl. Phys. Lett.* **2009**, *95*, 062909.
(22) Choi, T.; Lee, S.; Choi, Y. J.; Kiryukhin, V.; Cheong, S.-W. *Science* **2009**, *324*, 63−66.
(23) Ihlefeld, J. F.; Podraza, N. J.; Liu, Z. K.; Rai, R. C.; Xu, X.; Heeg, T.; Chen, Y. B.; Li, J.; Collins, R. W.; Musfeldt, J. L.; Pan, X. Q.; Schubert, J.; Ramesh, R.; Schlom, D. G. *Appl. Phys. Lett.* **2008**, *92*, 142908.
(24) Allibe, J.; Bougot-Robin, K.; Jacquet, E.; Infante, I. C.; Fusil, S.; Carrétéro, C.; Reverchon, J. L.; Marcilhac, B.; Creté, D.; Mage, J. C.; Barthélémy, A.; Bibes, M. *Appl. Phys. Lett.* **2010**, *96*, 182902.
(25) Wu, J. G.; Wang, J. *J. Am. Ceram. Soc.* **2010**, *93*, 2795−2803.
(26) Bi, L.; Taussig, A. R.; Kim, H.-S.; Wang, L.; Dionne, G. F.; Bono, D.; Persson, K.; Ceder, G.; Ross, C. A. *Phys. Rev. B* **2008**, *78*, 104106.
(27) Yuan, G. L.; Martin, L. W.; Ramesh, R.; Uedono, A. *Appl. Phys. Lett.* **2009**, *95*, 012904.
(28) Eerenstein, W.; Morrison, F. D.; Dho, J.; Blamire, M. G.; Scott, J. F.; Mathur, N. D. *Science* **2005**, *307*, 1203.
(29) Ederer, C.; Spaldin, N. A. *Phys. Rev. B* **2005**, *71*, 224103.
(30) Ju, S.; Cai, T. Y. *Appl. Phys. Lett.* **2009**, *95*, 231906.
(31) Rout, D.; Moon, K.-S.; Kang, S.-J. L. *J. Raman Spectrosc.* **2009**, *40*, 618−626.
(32) Yuan, G. L.; Or, S. W.; Chan, H. L. W.; Liu, Z. G. *J. Appl. Phys.* **2007**, *101*, 024106.
(33) Singh, S. K.; Ishiwara, H.; Maruyama, K. *Appl. Phys. Lett.* **2006**, *88*, 262908.
(34) Patterson, A. L. *Phys. Rev.* **1939**, *56*, 978−982.
(35) Hermet, P.; Goffinet, M.; Kreisel, J.; Ghosez, P. *Phys. Rev. B* **2007**, *75*, 220102.
(36) Jaiswal, A.; Das, R.; Maity, T.; Vivekanand, K.; Adyanthaya, S.; Poddar, P. *J. Phys. Chem. C* **2010**, *14*, 12432−12439.
(37) Zhang, S. T.; Lu, M. H.; Wu, D.; Chen, Y. F.; Ming, N. B. *Appl. Phys. Lett.* **2005**, *87*, 262907.
(38) Ramachandran, B.; Dixit, A.; Naik, R.; Lawes, G.; Rao, M. S. R. *Phys. Rev. B* **2010**, *82*, 012102.
(39) Yan, F.; Lai, M. O.; Lu, L.; Zhu, T. J. *J. Phys. Chem. C* **2010**, *114*, 6994−6998.
(40) Clark, S. J.; Robertson, J. *Appl. Phys. Lett.* **2009**, *94*, 022902.
(41) Djurisic, A. B.; Chan, Y.; Herbert, Li, E. *Mater. Sci. Eng., R* **2002**, *38*, 237−293.
(42) Li, W. W.; Zhu, J. J.; Wu, J. D.; Sun, J.; Zhu, M.; Hu, Z. G.; Chu, J. H. *ACS Appl. Mater. Interfaces* **2010**, *2*, 2325−2332.
(43) Jellison, G. E.; Modine, F. A. *Appl. Phys. Lett.* **1996**, *69*, 371−373.
(44) Yu, W. L.; Li, W. W.; Wu, J. D.; Sun, J.; Zhu, J. J.; Zhu, M.; Hu, Z. G.; Chu, J. H. *J. Phys. Chem. C* **2010**, *114*, 8593−8600.
(45) O'Donnell, K. P.; Chen, X. *Appl. Phys. Lett.* **1991**, *58*, 2924−2926.
(46) Pisarev, R. V.; Moskvin, A. S.; Kalashnikova, A. M.; Rasing, T. *Phys. Rev. B* **2009**, *79*, 235128.
(47) Wang, H.; Zheng, Y.; Cai, M.-Q.; Huang, H.; Chan, H. L. W. *Solid State Commun.* **2009**, *149*, 641−644.
(48) Hu, Z. G.; Li, W. W.; Wu, J. D.; Sun, J.; Shu, Q. W.; Zhong, X. X.; Zhu, Z. Q.; Chu, J. H. *Appl. Phys. Lett.* **2008**, *93*, 181910.
(49) Xu, X. S.; Brinzari, T. V.; Lee, S.; Chu, Y. H.; Martin, L. W.; Kumar, A.; McGill, S.; Rai, R. C.; Ramesh, R.; Gopalan, V.; Cheong, S. W.; Musfeldt, J. L. *Phys. Rev. B* **2009**, *79*, 134425.
(50) Varshni, Y. P. *Physica* **1967**, *34*, 149−154.
(51) Liu, B.; Cheng, C. W.; Chen, R.; Shen, Z. X.; Fan, H. J.; Sun, H. D. *J. Phys. Chem. C* **2010**, *114*, 3407−3410.
(52) Biernacki, S.; Scherz, U.; Meyer, B. K. *Phys. Rev. B* **1994**, *49*, 4501−4510.
(53) Fan, H. Y. *Phys. Rev.* **1951**, *82*, 900−905.
(54) Yakuphanoglu, F.; Arslan, M.; Küçükislamoğlu, M.; Zengin, M. *Sol. Energy* **2005**, *79*, 96−100.
(55) Selbach, S. M.; Tybell, T.; Einarsrud, M.-A.; Grande, T. *Chem. Mater.* **2007**, *19*, 6478−6484.
(56) Chen, P.; Xu, X.; Koenigsmann, C.; Santulli, A. C.; Wong, S. S.; Musfeldt, J. L. *Nano Lett.* **2010**, *10*, 4526−4532.
(57) Ramirez, M. O.; Kumar, A.; Denev, S. A.; Podraza, N. J.; Xu, X. S.; Rai, R. C.; Chu, Y. H.; Seidel, J.; Martin, L. W.; Yang, S. Y.; Saiz, E.; Ihlefeld, J. F.; Lee, S.; Klug, J.; Cheong, S. W.; Bedzyk, M. J.; Auciello, O.; Schlom, D. G.; Ramesh, R.; Orenstein, J.; Musfeldt, J. L.; Gopalan, V. *Phys. Rev. B* **2009**, *79*, 224106.